Aerosol versus Greenhouse Gas Effects on Tropical Cyclone Potential Intensity and the Hydrologic Cycle✐

Adam H. Sobel

Department of Applied Physics and Applied Mathematics, and Lamont-Doherty Earth Observatory, Columbia University, New York, New York

Suzana J. Camargo and Michael Previdi

Lamont-Doherty Earth Observatory, Columbia University, Palisades, New York

ABSTRACT

Aerosol cooling reduces tropical cyclone (TC) potential intensity (PI) more strongly, by about a factor of 2 per degree of sea surface temperature change, than greenhouse gas warming increases it. This study analyzes single-forcing and historical experiments from phase 5 of the Coupled Model Intercomparison Project, aiming to understand the physical mechanisms behind this difference. Calculations are done for the tropical oceans of each hemisphere during the relevant TC seasons, emphasizing multimodel means. PI theory is used to interpret the difference in the PI response to aerosol and greenhouse gas forcings in terms of three factors. The net surface turbulent heat flux (sum of the latent and sensible heat fluxes) explains half of the difference, thermodynamic efficiency explains at most a small fraction, and surface wind speed does not explain the remainder, perhaps because of the use of monthly mean data. Changes in turbulent surface heat fluxes are interpreted as responses to surface radiative flux changes in the context of the energy balance of the ocean mixed layer. Radiative kernels are used to estimate what fractions of the surface radiative flux changes are feedbacks due to temperature and water vapor changes. The greater effect of aerosol forcing occurs because shortwave forcing has a greater direct, temperature-independent component at the surface than does longwave forcing, for a forcing amplitude that provokes the same SST change. This conclusion recalls prior work on the response of precipitation to radiative forcing, and the similarities and differences between precipitation and potential intensity in this regard are discussed.

1. Introduction

This study addresses the effects of different radiative forcing agents on the potential intensity (PI) of tropical cyclones (TCs). PI is a theoretically derived quantity (Emanuel 1986, 1995; Bister and Emanuel 1998) that has been shown, with some caveats, to provide a useful upper bound to the intensities that TCs can achieve under given environmental conditions (e.g., Bryan and Rotunno 2009a,b). PI exerts a control on the average intensity of TCs even though most do not reach their PI (Emanuel 2000; Wing et al. 2007) [and some may exceed it, as discussed in several modeling studies, e.g., Persing and Montgomery (2003); Hausman et al. (2006); Bryan and Rotunno (2009b); Wang et al. (2014)], so that understanding radiative forcing of PI is relevant to understanding how radiative forcing affects actual TC intensities.

Several studies have pointed out that the cooling effect of aerosols should reduce PI, TC activity, or both, either over the North Atlantic (Mann and Emanuel 2006; Booth et al. 2012; Dunstone et al. 2013; Ting et al. 2015) or globally (Sobel et al. 2016). Inspired by the results of Ting et al. (2015) for the North Atlantic, Sobel et al. (2016) showed that in the multimodel mean of simulations from phase 5 of the Coupled Model Intercomparison Project (CMIP5) of the historical period, considering single-forcing (greenhouse gas-only or aerosol-only) experiments as well as those with all natural and anthropogenic forcings, aerosol-only effects were nearly equal and opposite to greenhouse gas-only

---

✐ Supplemental information related to this paper is available at the Journals Online website: https://doi.org/10.1175/JCLI-D-18-0357.s1.

Corresponding author: Adam H. Sobel, ahs129@columbia.edu

effects over most of the historical period, so that the net change in PI in the all-forcing experiments (where both forcings are present, and apparently behave approximately linearly) was small—at least until the most recent couple of decades, when greenhouse gas forcing begins to dominate. This is the case even though the greenhouse gas forcing is substantially larger in absolute terms (i.e., in $W\,m^{-2}$) over the historical period, so that the climate warms continuously. Sobel et al. (2016) interpreted this in light of the results of Emanuel and Sobel (2013), who showed in idealized single-column model (SCM) calculations that imposed changes in the solar constant induce larger changes in PI and precipitation, by approximately a factor of 2, than do changes in greenhouse gas forcing, when both are measured per degree of sea surface temperature (SST) change. To the extent that the SCM calculations can be taken to qualitatively represent the physics of the much more comprehensive CMIP5 models well enough for this problem, solar constant changes are an adequate proxy for aerosol forcing, and greenhouse gas forcing exceeds aerosol forcing in the CMIP5 models by something like a factor of 2 [as appears to be approximately true, e.g., Boucher et al. (2013)], then the results of Sobel et al. (2016) would be consistent with those of Emanuel and Sobel (2013). We do not attempt an analysis of the specific similarities and differences between the CMIP5 results and the single-column results of Emanuel and Sobel (2013), instead viewing the latter as providing a motivating hypothesis to be examined in the context of the more comprehensive CMIP5 simulations. In this study, we analyze the CMIP5 single-forcing experiments in greater detail, with the goal of further clarifying the physical mechanisms in that more comprehensive context.

Our analysis is closely related to recent studies of the global hydrological cycle. Greenhouse gas warming accelerates Earth's hydrologic cycle—increasing the rates of surface evaporation and precipitation—and aerosol cooling decelerates it. As in the case of PI, aerosols are about 2–3 times as effective in changing the hydrologic cycle per degree surface temperature change than are greenhouse gases (e.g., Feichter and Roeckner 2004; Liepert and Previdi 2009); this is relevant, for example, to proposed solar radiation management schemes for "geoengineering" (e.g., Bala et al. 2008). Some understanding of this difference has been gained by separating changes in the global energy budget into "fast" or "temperature-independent" and "slow" or "temperature-dependent" components (e.g., Andrews et al. 2009; O'Gorman et al. 2012; Samset et al. 2016). The temperature-independent radiative effect of a given forcing agent at the top of the atmosphere (TOA), or at the surface, is the change in the TOA or surface radiative flux that would occur in the absence of

any changes in the global mean surface temperature. In practice, the temperature-independent effect is often estimated as the change that occurs at the very beginning of a simulation in which the radiative forcing agent is switched on abruptly [e.g., using a "Gregory-type" approach (Gregory et al. 2004)], or by running a simulation in which the forcing agent is introduced and SSTs are held fixed. The temperature-dependent effect can be estimated as the change in radiative flux at equilibrium (or some other intermediate state in which there has been a finite temperature change) minus the temperature-independent effect. The temperature-dependent effect depends not only on surface temperature, but also on state variables related to it such as atmospheric temperature and water vapor. These influence TOA and surface radiation through feedbacks that have been extensively defined and documented in the literature, such as the water vapor feedback and lapse rate feedback. Studies with single forcings (e.g., Andrews et al. 2009; Previdi 2010; O'Gorman et al. 2012) show that these temperature-dependent feedbacks are similar for different radiative forcings. The temperature-independent effects of shortwave and longwave forcings, on the other hand, are different, and these differences lead to the differences in the hydrologic cycle response.

The different effects of shortwave and longwave forcings on the global hydrologic cycle can be understood either from the point of view of the tropospheric heat budget or the surface energy budget. In the global mean, over any time scale of interest for climate studies, the tropospheric heat budget requires that the vertically integrated radiative cooling of the atmosphere be balanced by the sum of latent heating due to water condensation and surface sensible heat flux. To the extent that sensible heat flux is small, then, the radiative cooling closely constrains precipitation (Allen and Ingram 2002).

The surface energy budget, on the other hand, requires that the sum of surface latent and sensible heat fluxes balance net surface radiation, after accounting for ocean heat transport and storage. In the global mean, the surface energy budget constrains precipitation as well, since precipitation and surface evaporation must balance on climatically relevant time scales. The relationship between the surface turbulent fluxes and potential intensity, on the other hand, is local. While our analysis bears considerable similarity to those in the hydrologic cycle literature, it differs in our focus on the tropics, and in particular on individual hemispheres of the tropics during the seasons in which TCs are most active. This local focus is facilitated by our use of the surface energy budget rather than the global heat budget. Particularly when considering only a single hemisphere and season at a time within the tropics as we do,

TABLE 1. CMIP5 models acronyms, number of ensembles and each simulations and period of the simulations used in our analysis. Information on the CMIP5 models and simulations can be found in Taylor et al. (2012). The periods of the historical, GHG and aerosols simulations are the same for each model. The climatologies are based on the ensemble mean 1861–1900 average, for the historical, GHG and aerosol simulations and 100 years for the preindustrial simulations (years 101–200). Models with an asterisk (*) do not have surface wind data available for our analysis.

Model	Period	Historical	GHG	Aerosols	Years	Preindustrial
CanESM2	1850–2005	5	5	5	996	1
CCSM4*	1850–2005	6	3	6	501	1
CESM1-CAM5*	1850–2005	3	3	3	319	1
CSIRO-Mk3.6.0*	1850–2005	10	5	5	500	1
FGOALS-g2*	1850–2005	5	1	1	700	1
GFDL CM3	1860–2005	5	3	3	500	1
GFDL-ESM2M	1861–2005	1	1	1	500	1
GISS-E2-H	1850–2005	10	5	10	240	1
GISS-E2-R	1850–2005	16	5	10	300, 401, 401	3
IPSL-CM5A-LR	1850–2005	5	6	1	1000	1
NorESM1-M	1850–2005	3	1	1	501	1

we anticipate that the energy transports due to the Hadley cell and extratropical eddies would make it challenging to interpret PI in terms of the atmospheric heat budget. The surface energy balance, though also not without complications (in this case due to ocean heat transport, as will be seen below), appears to us more straightforward. In any case, the local analysis yields results that are quantitatively, and in some respects even qualitatively different from those in the global mean. To illustrate this, we conclude our study with a direct comparison of tropical seasonal results with global annual mean results obtained using an analysis approach that is otherwise—that is, in all ways besides the averaging domain—identical to that used for the tropical results.

2. Models and data

a. Models

We consider here 11 CMIP5 models that have all the simulations and variables available that are necessary for our analysis. The names of the CMIP5 models, numbers of ensemble members and duration of each simulation are given in Table 1, and the simulations are described in Taylor et al. (2012). The historical simulations are forced with observed time-varying changes in all natural and anthropogenic forcings. The single forcing simulations that we consider are forced with greenhouse gases (GHG) only and aerosols only. The control simulation is the preindustrial quasi-equilibrium simulation.

The PI is calculated from monthly mean model data, following the definition of Bister and Emanuel (2002), using sea surface temperature, sea level pressure and profiles of temperature and humidity. The net radiative fluxes (shortwave and longwave) at the top of atmosphere

and surface were calculated as the difference of the downwelling and upwelling fluxes (i.e., radiative fluxes are positive down), while the surface latent and sensible heat fluxes are positive up. In these calculations the ratio of exchange coefficients for heat over momentum, $C_k/C_d = 0.9$; we assume reversible (as opposed to pseudoadiabatic) parcel ascent; dissipative heating is included (consistent with the theoretical discussion below); and the factor used to reduce the gradient wind at the top of the boundary layer to that at the 10-m level is 0.8.

For all variables and models, the monthly climatology is defined by the 1861–1900 ensemble mean of each simulation category (historical, GHG-only, or aerosol-only). The preindustrial climatology is defined using 100 years (years 101–200) of one ensemble member of that simulation. (For all models but one, only one ensemble member is available, so we use that number for all models in order to treat all models consistently.) The anomalies are calculated by subtracting the monthly climatological values for a given simulation from each of the individual ensemble members. The ensemble mean anomalies are defined as the mean of the anomalies over all ensemble members. Seasonal means are defined over the Northern Hemisphere peak TC season of August–October and the southern TC season of January–March. Area averages in each hemisphere are defined as 0°–30°N(S), including only ocean points. In the Southern Hemisphere, the longitudes 250°–360°E are excluded, as there are essentially no tropical cyclones in the southeast Pacific or South Atlantic. The global means that are shown are also annual means.

In most of this paper, we focus on multimodel means. Results from individual models are shown for some key quantities in the online supplemental material. These show that, to varying degrees, a substantial subset of the individual models—half or more in general, depending

to some extent on what quantity is examined—resemble the multimodel mean. Others show less coherent responses, that is, the trends in the quantities of interest are smaller compared to the variability. We conclude from this that the signals of interest here are, if not entirely robust across the ensemble, present in enough models so that the multimodel mean is worthy of study.

b. Radiative kernels

We compute surface radiative feedbacks due to temperature and water vapor changes in each simulation using the radiative kernel approach (Soden et al. 2008). Feedbacks are thus defined as

$$f_x = \frac{\partial R}{\partial x} \frac{dx}{dT_s} \equiv K_x \frac{dx}{dT_s}, \qquad (1)$$

where K_x is the radiative kernel quantifying the change in the surface radiation R due to an incremental change in the feedback variable x (either surface/atmospheric temperature or specific humidity), and dx and dT_s are the changes in the feedback variable and the tropical mean SST over the course of the simulation. We employ the radiative kernels of Previdi (2010) and Previdi and Liepert (2012) that were computed using an offline version of the radiation code from the ECHAM5 general circulation model (Roeckner et al. 2003). The climate response dx is calculated in each simulation as the difference in the monthly climatology between the periods 1861–1900 and 1981–2005, and is regridded to the ECHAM5 grid in order to have the same dimensions as the radiative kernels. The tropical mean SST change is the change between the same two time periods. In the results that follow, we present atmospheric temperature and water vapor feedbacks that have been vertically integrated from the surface to the tropopause. The tropopause height was computed from the models' 1981–2005 climatological mean temperature fields using the approach of Reichler et al. (2003). These vertically integrated feedbacks thus represent the net effect of tropospheric column temperature and water vapor changes on the surface radiation.

3. Results

Based on the results of Sobel et al. (2016) and Emanuel and Sobel (2013), we might expect the aerosol influence on PI per degree SST change to exceed that of greenhouse gases by approximately a factor of 2. This is demonstrated for the CMIP5 ensemble by Fig. 1, which shows multimodel mean time series of PI and SST for the Northern and Southern Hemisphere tropics from four sets of simulations: historical (all forcings), greenhouse

gas-only, aerosol-only, and preindustrial control. We see that the PI changes in the aerosol-only and greenhouse gas-only runs are approximately equal and opposite, while those in the historical runs—apart from the influence of several volcanoes, which appear as negative excursions lasting a few years—show little trend, at least until the last few decades. In SST, the increases in the greenhouse gas-only simulations clearly exceed in magnitude the decrease in the aerosol-only simulations by about a factor of 2, and the historical simulations show an increasing trend over the whole twentieth century, though disrupted somewhat by several volcanoes late in the century. Individual models, as might be expected, produce noisier time series than the multimodel means, and some range in their responses to the forcings (supplemental material, Figs. 1 and 2), but do not overall change our impression derived from the multimodel mean.

An interesting feature of Fig. 1 is that, in the aerosol-only case, the changes in the Southern Hemisphere in both PI and SST are, though smaller than those in the Northern Hemisphere, perhaps not as small as we might have expected. We will show below that these Southern Hemisphere changes can be explained in terms of surface radiative changes to a similar degree as those in the Northern Hemisphere, but the question will remain why the Southern Hemisphere radiative changes are as large as they are. Based on the results of Shindell et al. (2013) or Boucher et al. (2013) on a specific set of models, for example, we expect the "effective aerosol forcing" to be much larger in the Northern than the Southern Hemisphere, particularly when the southeast Pacific and South Atlantic are excluded. We do not have a simple explanation for this at present, but we do note that the effective aerosol forcing in the above-mentioned studies is computed offline using fixed surface temperature, and thus does not express the full response of the coupled system (including, in particular, changes to the large-scale circulation of the atmosphere, with attendant cloud changes that can affect radiation) while the latter is what is shown here, and also that the set of models and simulations here are not identical to those for which the effective radiative forcings were computed by Shindell et al. (2013) or Boucher et al. (2013). A more in-depth analysis of the cause of the Southern Hemisphere radiative changes would require knowledge of the specific aerosol forcings used in the models analyzed here. While we show results from both hemispheres below, our greater interest is in the Northern Hemisphere, since both the number of tropical cyclones and the aerosol forcing are greater there.

As our goal here is to understand the different responses of PI and SST to forcing, it is helpful to look at the relationships between these (and other) variables, taking out the time dimension. Figure 2 shows
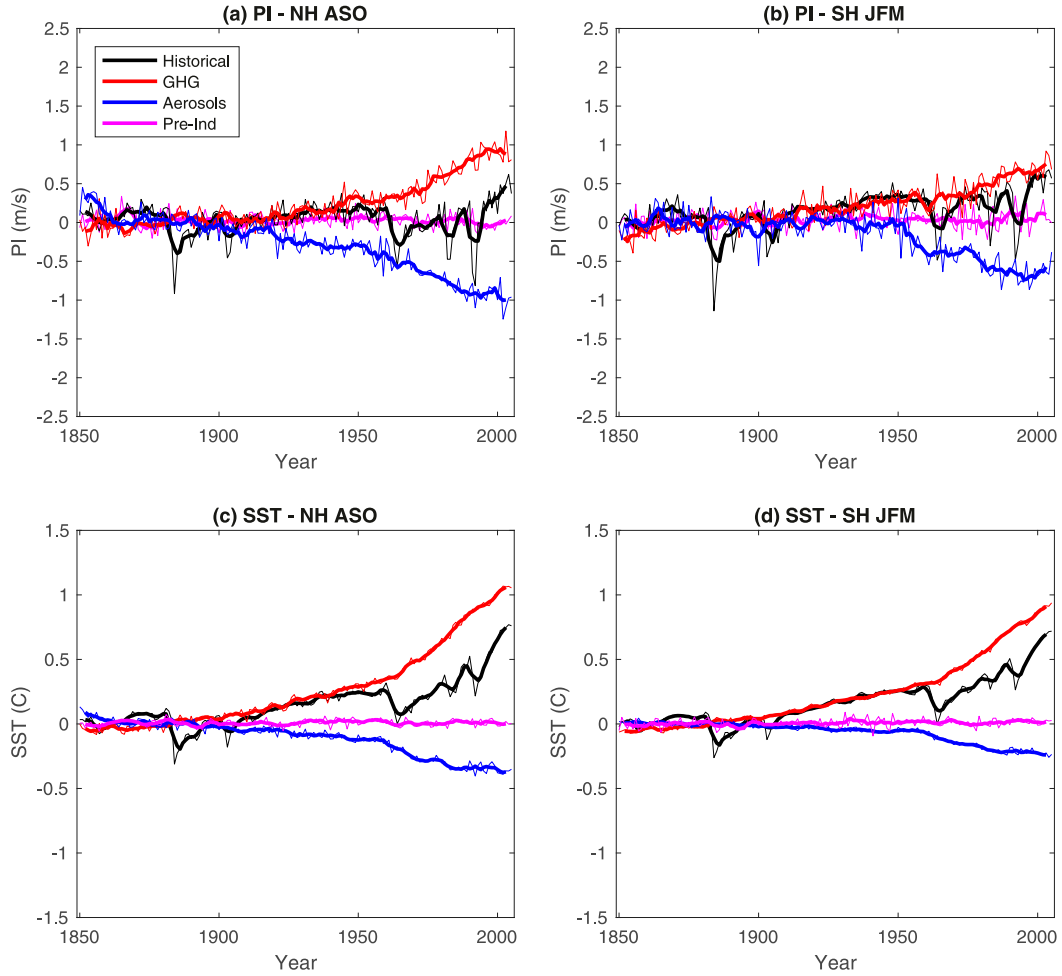
FIG. 1. Time series of multimodel mean (a),(b) potential intensity and (c),(d) sea surface temperature anomalies in the (a),(c) Northern Hemisphere tropics and (b),(d) Southern Hemisphere tropics. Greenhouse gas-only experiments are in red, aerosol-only experiments in blue, and historical experiments in black. Thick lines are 5-yr running means, thin lines annually varying values.

scatterplots produced from the multimodel mean data, averaged in the same way as in Fig. 1; each point is a different time from the time series. Figures 2a and 2b scatter SST against PI for August–September–October (ASO) and January–February–March (JFM), and show, as expected, a slope greater in the aerosol-only simulation than the greenhouse gas-only simulation, by about a factor of 2.5. In the remainder of the paper, we show a number of such scatterplots. Regression slopes are indicated on the plots themselves, while R^2 values are shown, along with the regression slopes, in Table 2.

To understand the response of PI to forcing, we consider that, according to theory, PI can be computed as a function of the enthalpy disequilibrium at the surface:

$$V_p^2 = \frac{T_s - T_o}{T_o}\frac{C_k}{C_D}(k^* - k_{RMW}),\qquad(2)$$

where V_p is the PI; T_s is the SST and T_o is the outflow temperature; C_k and C_D are bulk exchange coefficients for heat and momentum, respectively; and k^* and k_{RMW} are the saturation moist enthalpy of the sea surface and the actual enthalpy of near-surface air in the tropical cyclone eyewall, respectively. Equation (2) is from Bister and Emanuel (1998) and includes the effect of dissipative heating, so that the denominator contains T_o rather than T_s. The computational algorithm we use to calculate PI does not use (2), but rather a theoretically equivalent expression involving convective available potential energy (CAPE) from Bister and Emanuel [2002, their Eq. (3)].

The eyewall value k_{RMW} is not, in general, equal to the ambient value, but according to Emanuel and Rotunno (2011), the PI computed from (2) and that which would be obtained with the ambient air-sea disequilibrium are

(a) PI vs. SST - NH ASO

Slopes:
0.60
0.93
2.33

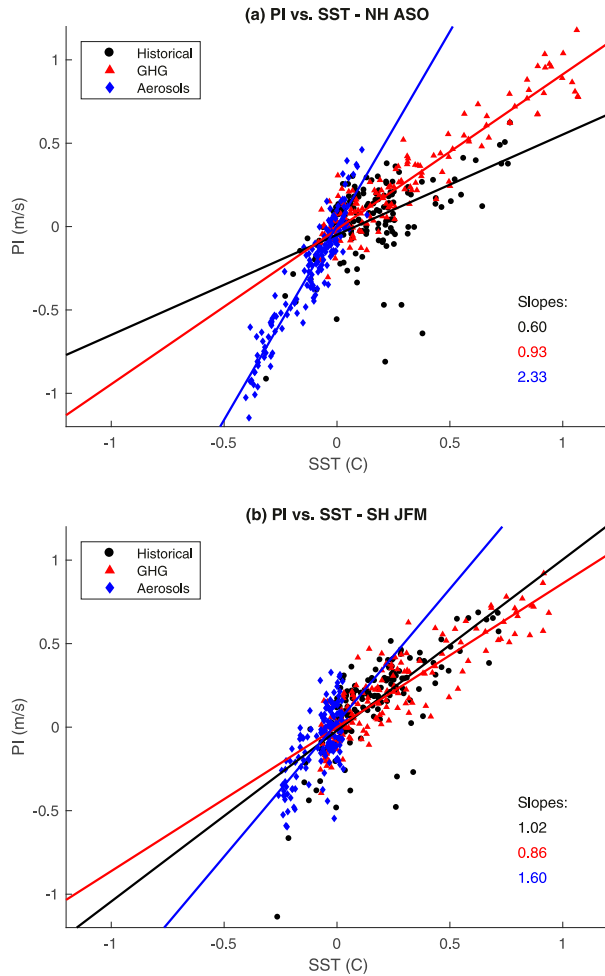**(b) PI vs. SST - SH JFM**

Slopes:
1.02
0.86
1.60

FIG. 2. The same data as in Fig. 1, but in the form of scatterplots of SST (horizontal axis) vs potential intensity (vertical axis): (a) Northern Hemisphere and (b) Southern Hemisphere. Least squares regression lines are plotted in the same colors as the associated data, and slopes are given in the lower-right area of the plot.

related by a multiplicative constant, call it here γ, which is a function of the ratio of exchange coefficients. Thus if we denote the actual ambient value of the moist enthalpy of surface air as k, (2) can be written as

$$V_p^2 = \frac{T_s - T_o}{T_o} \frac{C_k}{C_D} \gamma(k^* - k). \qquad (3)$$

Since the turbulent enthalpy flux F_{turb}, sum of the latent and sensible components E and H, can be written as

$$F_{\text{turb}} = E + H = C_k \rho |\mathbf{V}|(k^* - k),$$

where $\mathbf{V}$ is the surface wind speed and ρ is the density of near-surface air, it follows that (2) can be written as

$$V_p^2 = \frac{T_s - T_o}{T_o} \frac{\gamma F_{\text{turb}}}{C_D \rho |\mathbf{V}|}, \qquad (4)$$

or, assuming the ocean mixed layer is in energy balance (e.g., Emanuel 2007),

$$V_p^2 = \frac{T_s - T_o}{T_o} \frac{\gamma(F_{\text{rad}} + F_{\text{oc}})}{C_D \rho |\mathbf{V}|}, \qquad (5)$$

where F_{rad} is the net (shortwave plus longwave) downward radiative flux into the surface and F_{oc} is the net convergence of ocean heat transport into the mixed layer.

Our interest here is in radiatively forced perturbations that are small in comparison to the absolute values of quantities of interest. For any quantity X, we can write $X = \overline{X} + X'$, where $\overline{X}$ is the preindustrial mean and X' is a forced perturbation. We also introduce the notation $\eta = (T_s - T_o)/T_o$ for compactness. If the ratios $V_p'/\overline{V_p}$, $\eta'/\overline{\eta}$, $|\mathbf{V}|'/|\overline{\mathbf{V}}|$, and $F_{\text{turb}}'/\overline{F}_{\text{turb}}$ are all small—that is, the long-term changes in all quantities are small compared to their total values in the time mean—then we can write, based on (4):

$$V_p^2 \approx \overline{V_p^2}\left(1 + \frac{\eta'}{\overline{\eta}} + \frac{F_{\text{turb}}'}{\overline{F}_{\text{turb}}} - \frac{|\mathbf{V}|'}{|\overline{\mathbf{V}}|}\right), \qquad (6)$$

or

$$\frac{2V_p'}{\overline{V_p}} \approx \frac{\eta'}{\overline{\eta}} + \frac{F_{\text{turb}}'}{\overline{F}_{\text{turb}}} - \frac{|\mathbf{V}|'}{|\overline{\mathbf{V}}|}. \qquad (7)$$

We use (7) to understand the factors influencing PI change in the radiatively forced experiments. Figure 3 shows time series of PI, $F_{\text{turb}}'/\overline{F}_{\text{turb}}$, $\eta'/\overline{\eta}$, and $-|\mathbf{V}|'/|\overline{\mathbf{V}}|$. The values of all are on the order of 1%, justifying the use of small perturbation expansions. The other three terms on the right-hand side should, per theory above, add up to twice the PI, but do not. Only the surface heat fluxes, F_{turb}, show very similar behavior to the PI, but with equal magnitude (as opposed to twice the PI), so that they explain only half of the signal. The thermodynamic efficiency, η, varies in the right sense to explain some of the remaining signal, but is too small to do so, especially in the greenhouse gas case, where it varies almost not at all. Examination of the individual models (Fig. S6 in the online supplemental material) also shows that the signal in η is due to only a couple of models, so it should not be taken too seriously. The surface wind speed, on the other hand, has significant variations, but they are quite noisy, and lack a long-term trend. There do appear to be substantial changes near the end of the period, but these are of the wrong sign to explain the missing PI change; the wind speed decreases (which would tend to increase PI) in

TABLE 2. Slopes and coefficients of determination (R^2) for MMM linear regressions in the tropical Northern Hemisphere (NH), Southern Hemisphere (SH), and globally for historical (Hist), greenhouse gases (GHG), and aerosol (Aeros) simulations. The slopes are also given in the figures, though the R^2 values are not.

	Northern Hemisphere			Southern Hemisphere			Global		
	Hist	GHG	Aeros	Hist	GHG	Aeros	Hist	GHG	Aeros
				PI vs SST (Fig. 2)					
Slope	0.60	0.93	2.33	1.02	0.86	1.60			
R^2	0.26	0.88	0.89	0.54	0.76	0.44			
			Surface longwave + shortwave vs latent heat + sensible heat (Figs. 4 and 10a)						
Slope	0.48	0.53	0.68	0.52	0.69	0.84	0.32	0.53	0.73
R^2	0.47	0.63	0.80	0.59	0.64	0.60	0.46	0.99	0.99
				PI vs latent heat + sensible heat (Fig. 5)					
Slope	1.04	1.22	2.01	1.43	1.67	1.76			
R^2	0.17	0.56	0.73	0.47	0.51	0.30			
				SST vs latent heat flux (Figs. 6a,b and 9a)					
Slope	0.16	2.01	5.67	1.81	2.66	6.73	0.52	0.97	1.95
R^2	0.004	0.86	0.87	0.35	0.84	0.73	0.53	0.99	0.53
				SST vs sensible heat flux (Figs. 6c,d and 9b)					
Slope	−0.91	−0.65	−0.31	−0.77	−0.69	−0.31	−0.44	−0.21	0.14
R^2	0.84	0.95	0.42	0.84	0.94	0.20	0.79	0.95	0.56
				SST vs longwave surface (Figs. 6e,f and 9c)					
Slope	4.23	3.37	2.22	4.39	3.68	2.55	1.91	1.26	0.32
R^2	0.95	0.99	0.87	0.94	0.98	0.66	0.91	0.99	0.62
				SST vs shortwave surface (Figs. 6g,h and 9d)					
Slope	−3.97	−0.97	5.11	−2.23	−1.14	4.29	−0.93	0.15	2.52
R^2	0.38	0.61	0.83	0.19	0.43	0.50	0.25	0.67	0.95
				SST vs longwave TOA (Figs. 11a,c,e)					
Slope	2.08	1.08	−1.11	2.48	1.10	−3.62	0.50	−0.30	−1.84
R^2	0.37	0.74	0.31	0.42	0.61	0.58	0.14	0.87	0.96
				SST vs shortwave TOA (Figs. 11b,d,f)					
Slope	−0.78	0.43	4.18	0.32	0.36	3.98	0.09	0.71	2.3
R^2	0.03	0.28	0.83	0.005	0.10	0.56	0.002	0.98	0.95

the aerosol case, and increases (which would tend to decrease PI) in the greenhouse gas case; note that the wind speed term is plotted with a minus sign, consistent with the way it appears in (7). Examination of the individual models (Fig. S7) shows little evidence of consistent trends in multiple models, and thus further suggests that the changes in surface wind speed are, for our purposes, noise.

The surface wind speed we use is that computed from monthly mean data for the separate wind components, and thus lacks higher-frequency variability. The wind speed that is important for the PI is the total wind speed, including variability at all frequencies, since that is what controls the surface fluxes. It is possible that the results could change substantially, even qualitatively, with the inclusion of submonthly winds. We did not have access to daily winds here; further, it is possible that even daily winds would not be adequate. To be sure to quantify the effects of wind speed properly, one should compute the mean of the actual wind speed, with the magnitude taken at each time step. Further, one should consider

how the boundary layer scheme in each model uses the wind speed in the bulk formulas for the latent and sensible heat fluxes; the wind speed used for this purpose may not be simply the model-simulated wind speed, but may incorporate gustiness factors or other parameterizations to account for subgrid-scale variability. An additional challenge is that we may expect high-frequency wind variations to be among the less robust quantities across the multimodel ensemble, given the high degree of variation across that ensemble in how subseasonal variability overall is simulated (e.g., Hung et al. 2013).

Nonetheless, despite all the complications, and the half of the signal in PI that remains unexplained, the results of Fig. 3 suggest that understanding the surface flux changes is, at least, a useful step in understanding PI. Another fact in support of this view is that, of the quantities on the RHS of (7), F_{turb} is the most straightforwardly related to radiative forcing, since the turbulent fluxes and radiative fluxes both participate directly in the heat budget of the ocean mixed layer. Thus we
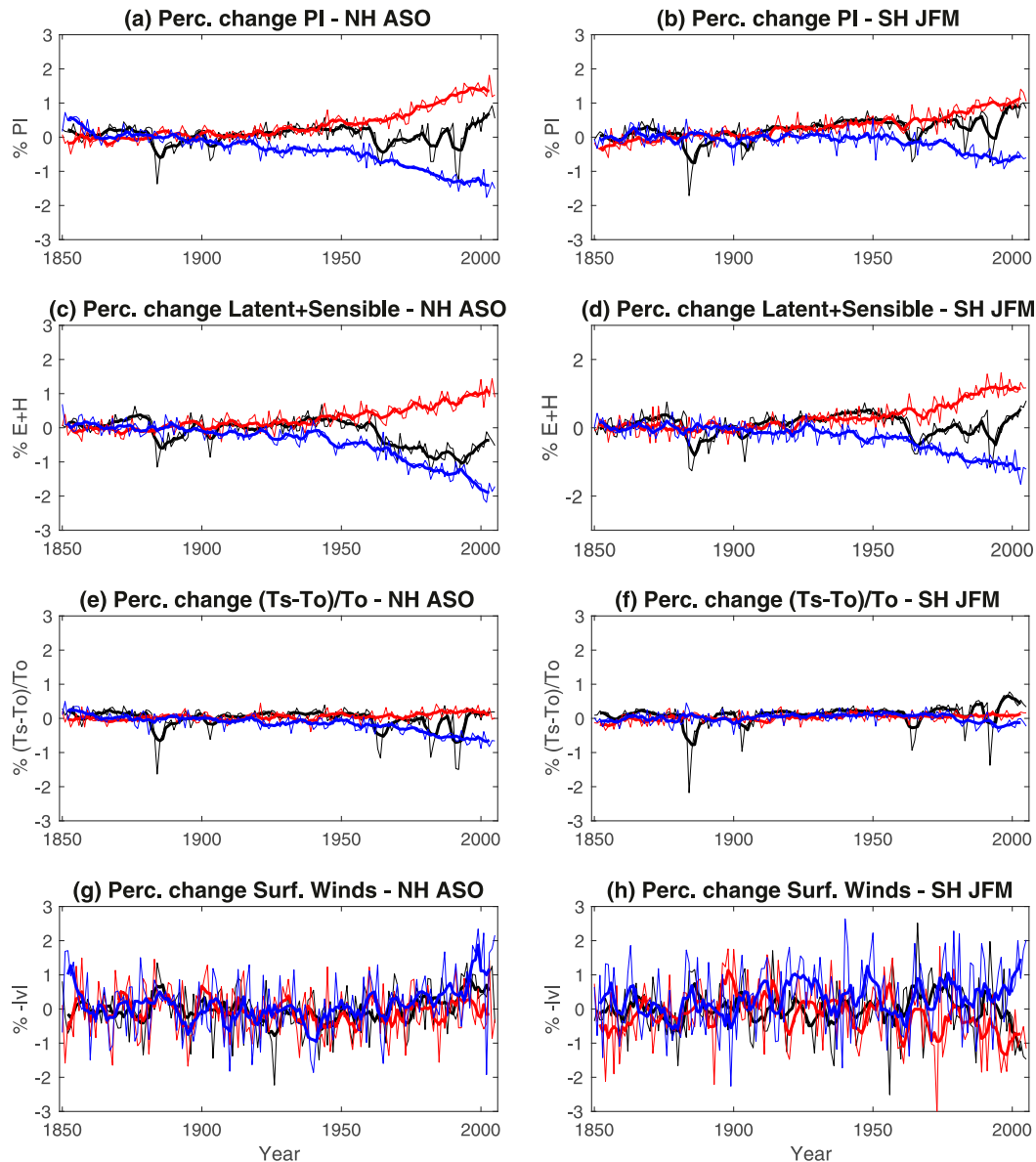
FIG. 3. Multimodel mean (a),(b) percentage changes in potential intensity, (c),(d) sum of surface latent and sensible heat fluxes, (e),(f) thermodynamic efficiency [$(T_s − T_o)/T_o$], and (g),(h) surface wind speed for the (left) Northern and (right) Southern Hemispheres.

interpret the surface turbulent flux changes as providing an explanation for part—specifically, about half—of the PI changes. Further investigation of the other factors influencing PI, especially the wind speed influence, is left for future work. This would probably be best carried out with a single model, using new experiments in which the wind speed can be saved at high frequency and the boundary layer scheme interrogated directly in order to be sure that the quantities from the model are being interpreted consistently with their use in the PI algorithm.

In what follows, we will interpret changes in surface radiative fluxes as causing changes in surface turbulent fluxes (and thus, by the arguments above, PI). The two are related by (5), but that also contains the ocean heat transport term. This term represents the net ocean heat transport into the mixed layer, both in the vertical and horizontal. [To derive (5) one must assume that the ocean mixed layer is in energy balance on the time scales of interest, but the deep ocean need not be, as there can be a vertical flux through the bottom of the mixed layer.] Figure 4 shows scatterplots of the net turbulent surface heat flux versus the net radiative
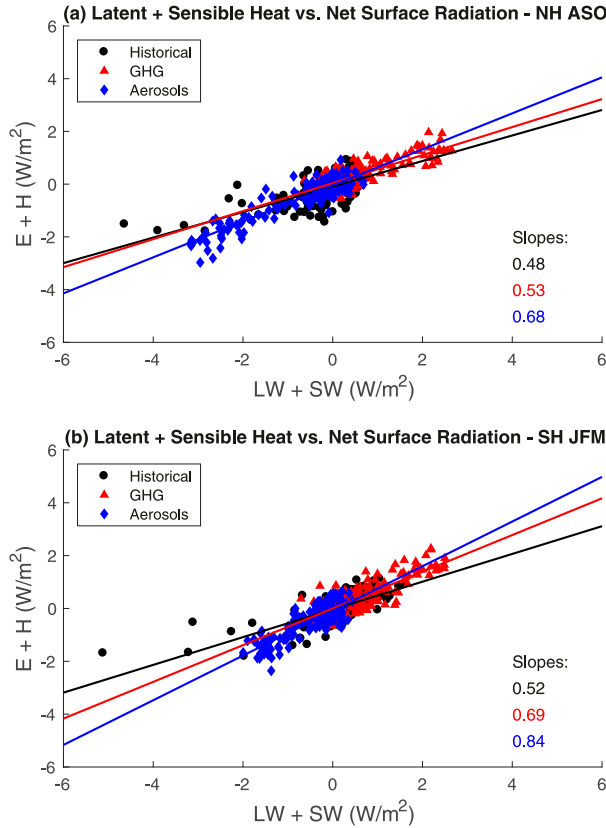
FIG. 4. As in Fig. 2, but for the net surface radiative flux (shortwave plus longwave; horizontal axis) vs the sum of latent and sensible heat fluxes (vertical axis).

flux. If the ocean heat transport term were negligible, we would expect a strong correlation with a slope of 1. The correlation is indeed strong, but the slope is less than 1. Focusing on the single-forcing experiments, the slopes in the Northern Hemisphere are 0.53 (GHG) and 0.68 (aerosol), and in the Southern Hemisphere are 0.69 (GHG) and 0.84 (aerosol). The fact that the slopes are less than 1 indicates that some of the heat added by radiative forcing at the top of the mixed layer is exported, either vertically to the deep ocean, horizontally to higher latitudes or the other hemisphere, or likely both. Given the tight correlation, Fig. 4 suggests a parameterization of the ocean heat transport term such that (5) is approximated by

$$V_p^2 = \frac{T_s - T_o}{T_o} \frac{\gamma \alpha F_{\text{rad}}}{C_D \rho |\mathbf{V}|}, \qquad (8)$$

where α is the slope found empirically in Fig. 4. That heat transport from the mixed layer to the deep ocean can be parameterized with some success as proportional to radiative forcing has been shown previously (e.g., Gregory and Forster 2008; Held et al. 2010). Equation (8) expresses the same idea in a slightly different context, being hemispheric
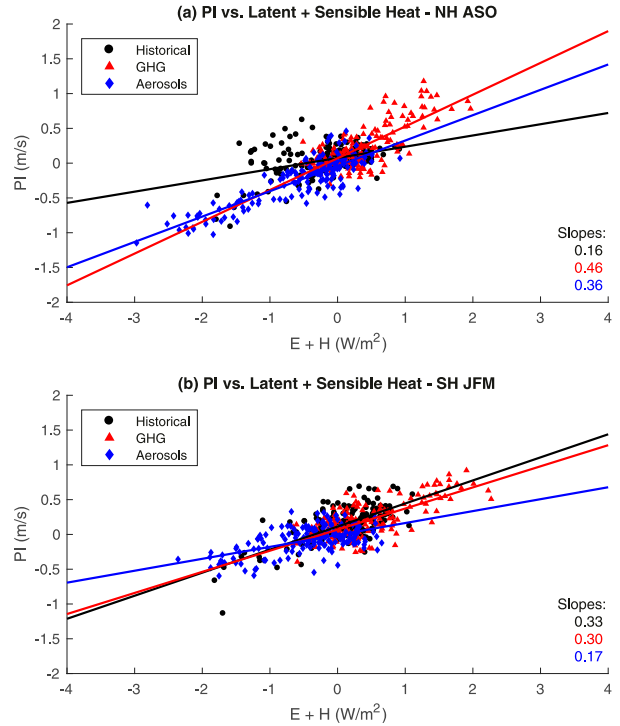

FIG. 5. As in Fig. 2, but for the sum of latent and sensible heat fluxes (horizontal axis) vs potential intensity (vertical axis).

rather than global and considering surface rather than top-of-the-atmosphere forcing. We do not have an explanation for the quantitative differences in α either between the hemispheres, or the different forcings. The fact that it is larger for aerosol than GHG forcing in both hemispheres is interesting, and explains a modest fraction of the aerosol–GHG difference in the PI change per unit SST change. But since the latter is a factor of 2 while the difference in α (at least if we consider each hemisphere separately) is considerably smaller, it remains relevant to examine the differences in the surface radiative fluxes, and to consider them the primary driver of the different PI response, as the analysis below will support.

An additional interesting (if challenging) feature of the results is that both the radiative flux changes and the PI changes are larger than the turbulent flux changes, so that our interpretation would be more quantitatively successful if we could link the two directly (i.e., if the ocean transport term were to vanish). Yet that is not the case, so the fact that the changes are smaller than those in PI remains an unsolved problem for future research.

We proceed to examine how and why changes in surface radiative fluxes differ between aerosol-only and greenhouse gas-only experiments, and take those to explain changes in the surface turbulent fluxes. Figures 5a and 5b scatter PI against the sum of latent and sensible heat flux F'_{turb}. Both quantities are in physical units, for easier comparison
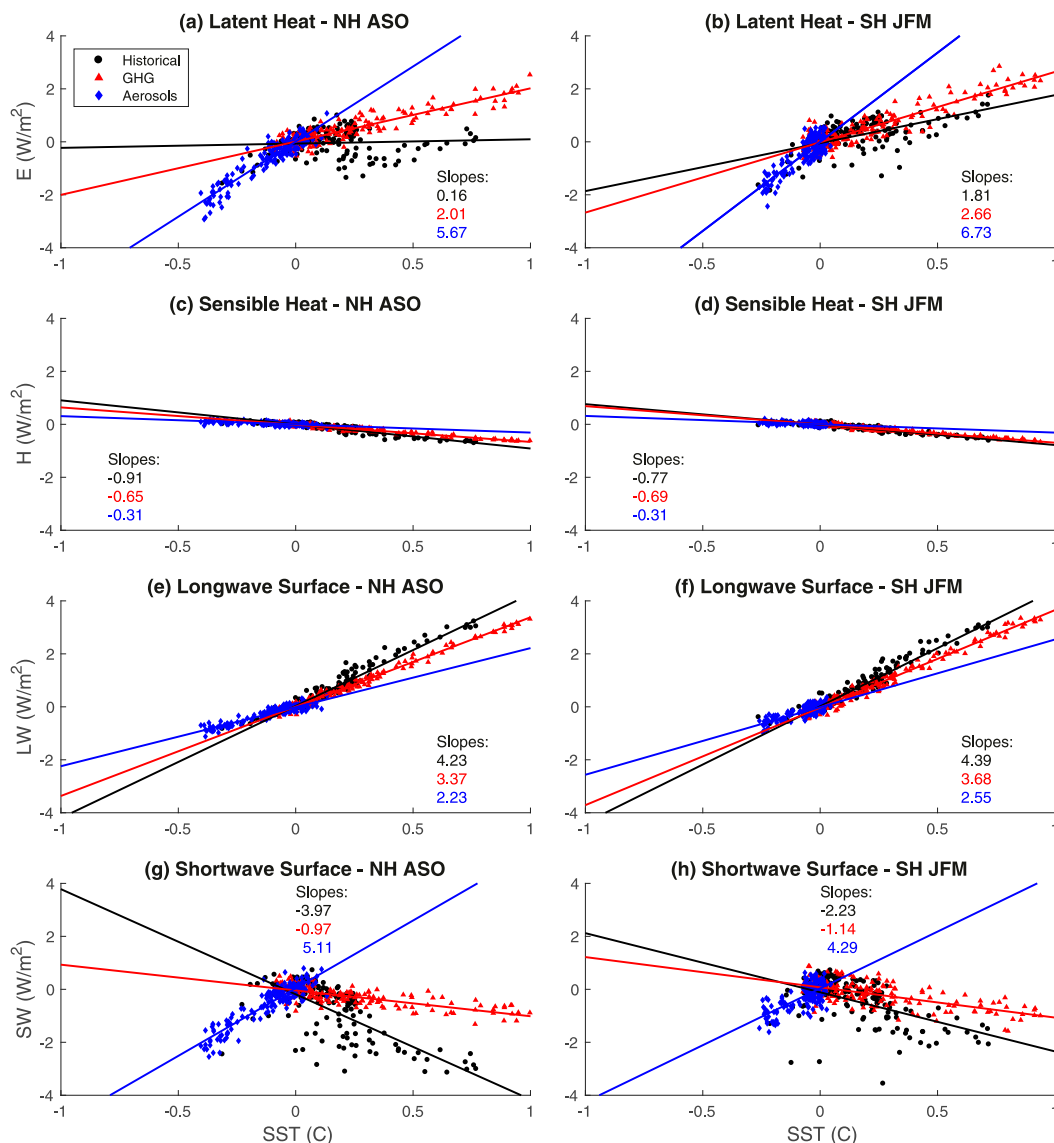
FIG. 6. Scatterplots of multimodel mean surface energy fluxes vs SST as in Fig. 2. Results for (left) the Northern Hemisphere tropics in ASO and (right) the Southern Hemisphere tropics in JFM. Quantities plotted on the vertical axis are (a),(b) latent heat flux; (c),(d) sensible heat flux; (e),(f) net longwave radiative flux, and (g),(h) net shortwave radiative flux. Color scheme denotes different experiments as in previous figures.

to other figures. Normalizing the perturbations by their climatological means gives, as Fig. 3 leads us to expect, a slope about half as large as it would be if the turbulent fluxes explained all the PI changes expected per theory—that is, if the thermodynamic efficiency and surface wind speed contributions were zero. Figures 6a–h show analogous scatterplots of terms in the surface energy budget—latent heat flux, sensible heat flux, longwave radiative flux, and shortwave radiative flux—versus SST, for both the Northern and Southern Hemisphere tropics in the respective TC seasons. Thus in perfect energy balance, the sum of sensible and latent fluxes would equal the sum of the radiative

fluxes. As expected given the results shown in Fig. 4, the slopes derived from linear regression do not balance in this way, presumably due to ocean heat transport and storage. There is an imbalance of $\sim 1.1 \, \mathrm{W \, m^{-2} \, K^{-1}}$ for the GHG case and $0.9 \, \mathrm{W \, m^{-2} \, K^{-1}}$ for the aerosol case in the Northern Hemisphere for ASO, with the corresponding numbers being 0.6 and $2.2 \, \mathrm{W \, m^{-2} \, K^{-1}}$ for the Southern Hemisphere in JFM. Nonetheless, the substantial difference in the latent heat flux – SST relationship between the aerosol and greenhouse gas experiments is well explained qualitatively, and to a reasonable extent even quantitatively, by the difference in the radiative terms in those experiments.
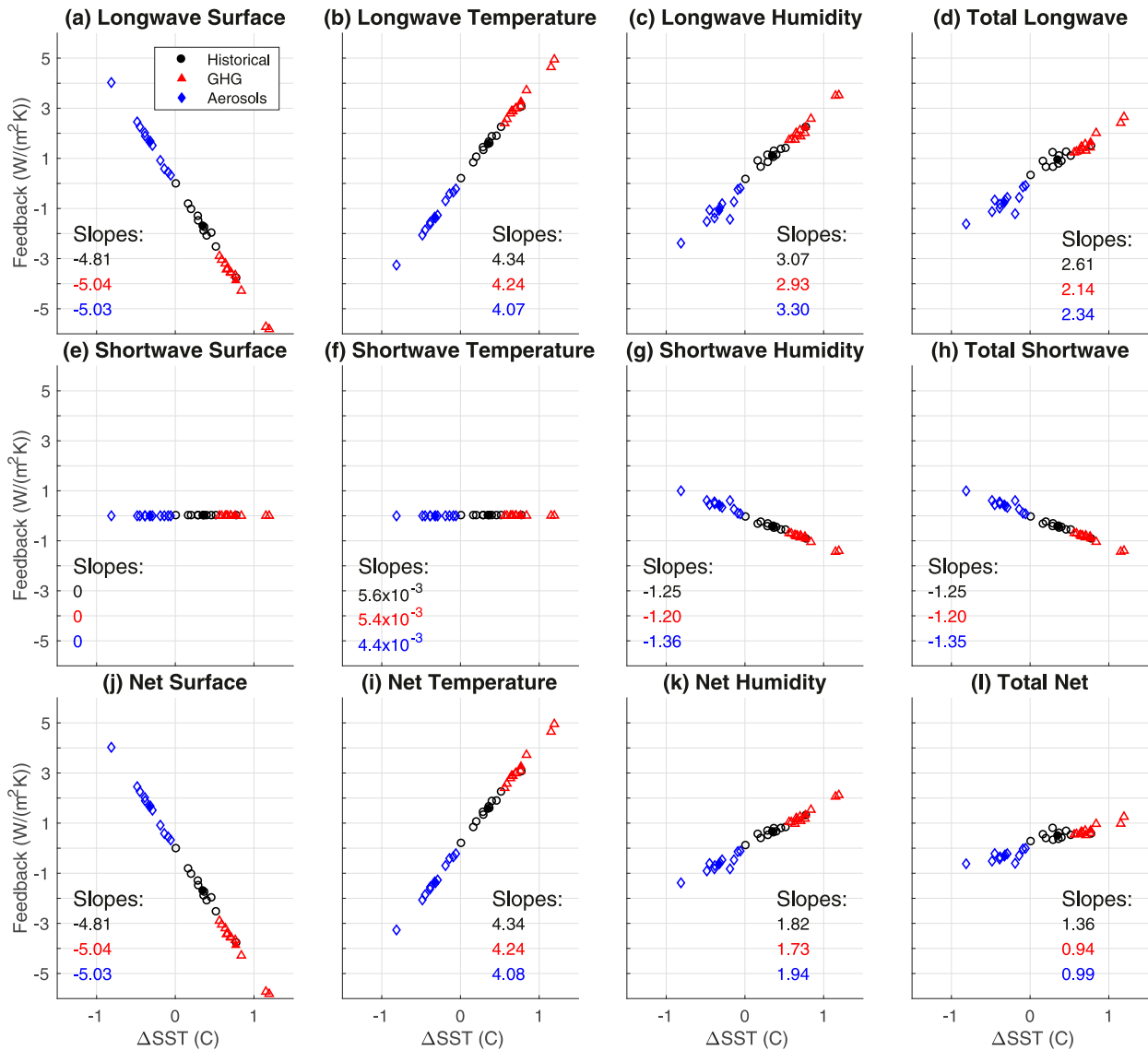
FIG. 7. Feedbacks computed by radiative kernels. Color scheme denotes different experiments as in previous figures. Each open symbol corresponds to the ensemble mean of an individual model, while solid symbols denote multimodel means.

Summing the slopes from the radiative terms gives $\sim 7\,\mathrm{W\,m^{-2}\,K^{-1}}$ for the aerosol versus $2.5\,\mathrm{W\,m^{-2}\,K^{-1}}$ for the GHG experiments, while the sum of the latent and sensible heat flux slopes is $\sim 5\,\mathrm{W\,m^{-2}\,K^{-1}}$ for the aerosol versus $\sim 1.5\,\mathrm{W\,m^{-2}\,K^{-1}}$ for the GHG experiment. A similar degree of agreement is obtained for the historical experiments as well, though the scatter is greater and there is much more cancellation between the two radiative terms. This is roughly consistent with our expectation that the historical experiments can be thought of as a linear sum of the aerosol and GHG experiments (e.g., Marvel et al. 2015, or see Fig. 1).

Focusing on the difference between the aerosol and GHG results, we see that the longwave flux into the ocean increases slightly more slowly with SST for the aerosol than for the GHG forcing in the Northern Hemisphere (though not the Southern Hemisphere). The difference in the shortwave is much more dramatic, with the shortwave flux into the ocean increasing strongly with SST for the aerosol experiment while it decreases weakly in the GHG experiment, perhaps due to increased shortwave absorption by water vapor.

The radiative flux changes can be thought of as having a "direct" component due to the radiative forcing agent (aerosols or greenhouse gases) as well as a "feedback" component resulting from temperature and moisture changes. We use radiative kernels to estimate the latter. Figure 7 shows feedbacks computed from the
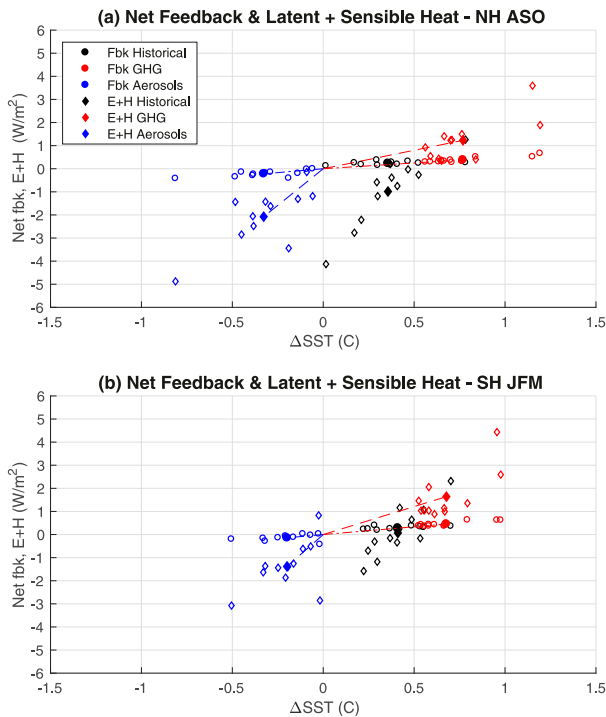
FIG. 8. Changes in net turbulent surface flux (diamonds) and the same quantity estimated from the kernel feedbacks only (circles); all values are differences between periods at the end and beginning of the simulations (see text for details). Individual models are open symbols and filled symbols are multimodel means. Color scheme as in previous figures and shown in legend. Lines are drawn between the origin and the multimodel mean single-forcing results (dashed) and kernel feedbacks (diamonds) as discussed in the text.

radiative kernels from the ensemble means of the three sets of experiments, labeled as in the previous figures. Each of the first three columns shows the changes in surface radiative fluxes—longwave, shortwave, and net or the sum of shortwave and longwave (top, middle, and bottom rows, respectively)—computed from the changes in a single input variable. The first column shows changes due to surface temperature only, while the second and third show changes due to atmospheric temperature and humidity changes only. The last column shows the sum of all three components, giving the kernel's estimates of the total changes in surface radiative fluxes resulting from temperature and water vapor changes.

Given the feedbacks, the remainder of the radiative flux changes at the surface can be considered the direct response to radiative forcing agents (greenhouse gases and aerosols). In Fig. 8 we separate these two components, as follows. We use the kernel calculations shown in Fig. 7 to estimate the feedbacks. Then, since the feedbacks represent radiative fluxes, but we are comparing them to turbulent fluxes in this figure, we multiply the feedbacks by the slopes from the relevant

experiments found in Fig. 4, which represent the fraction of radiative flux change that is balanced by turbulent flux change (as opposed to ocean heat transport and storage). That is, we assume that the ratio between radiative flux changes and turbulent flux changes is the same for the feedback component as for the total changes. All quantities shown are values from the late historical period (1981–2005) minus those in the early historical period (1861–1900). Each diamond-shaped symbol indicates changes in SST (horizontal axis) and net latent plus sensible heat flux (vertical axis) for a single model, with colors indicating different experiments as above. The slopes of the lines connecting these multimodel means (solid diamonds) to the origin can be interpreted similarly to the slopes of the scatterplots in Fig. 5. The circles indicate what the changes in latent plus sensible heat flux would be if they were responses to the radiative flux changes inferred from the kernels. That is, we assume in this figure both that the kernels accurately capture the feedbacks due to temperature and humidity changes and that, as described above, the changes in radiative fluxes are balanced by changes in turbulent fluxes in the same proportion whether we are considering total changes or just the feedback component. Under these assumptions, the differences between the circles and the diamonds represent the direct effects of the radiative forcings. In practice, the multiplication of the feedbacks by the slopes from Fig. 4 makes little difference to our conclusions, since the feedback component is small compared to the total changes even before that multiplication, so that the direct component is dominant regardless.

We see from Fig. 8 that not only are the changes in surface turbulent heat fluxes per degree SST change considerably larger for aerosol-only than greenhouse gas-only experiments, but even more so, the components of those changes that we infer to be directly radiatively forced—the difference between the total and the feedback, diamond minus circle—are as well. The feedbacks, on the other hand—apparent here as the slopes of the lines connecting the circles to the origin—are similar between the multimodel means of the greenhouse gas-only and aerosol-only experiments, at least in the Northern Hemisphere. We interpret the directly forced change as being driven by the component of the surface radiative flux change that results from the aerosols or greenhouse gases alone; this is referred to as the temperature-independent component of the climate response in many studies of the global hydrologic cycle (Andrews et al. 2009, O'Gorman et al. 2012). That this component is larger for shortwave (aerosol) than longwave (greenhouse gas) forcings is consistent with those studies, as is the similarity in the temperature-dependent feedbacks, though these prior studies consider global and
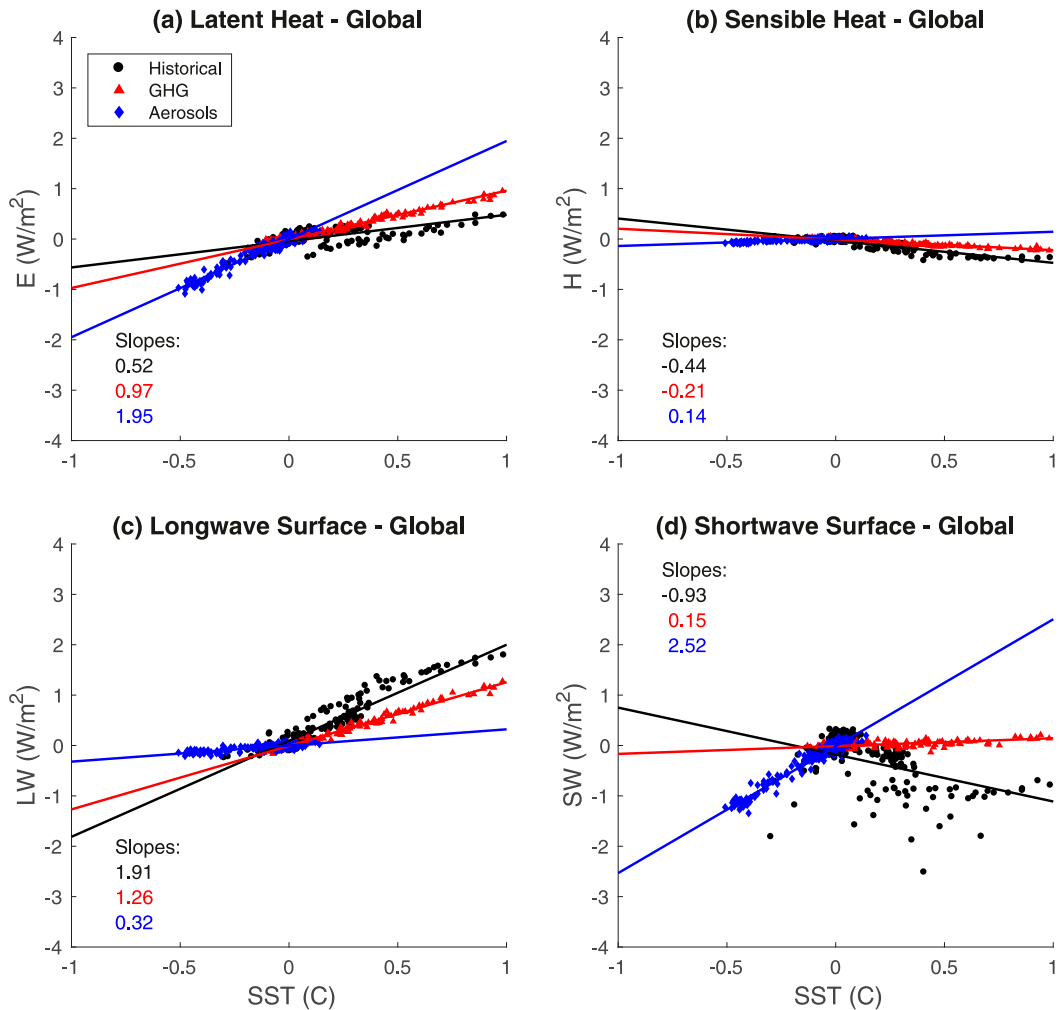
FIG. 9. Scatterplots of longwave and shortwave surface fluxes vs SST in the global and annual mean.

annual means while we consider changes over the tropical oceans of single hemispheres in single seasons.

To make a closer connection to the literature on the global hydrologic cycle, Figs. 9 and 10 are analogous to Figs. 6 and 8 except that they show global and annual means. The results in Figs. 9 and 10 bear some qualitative similarity to those in Figs. 6 and 8, particularly in that the total turbulent flux changes per degree SST are larger for aerosol than greenhouse gas forcing. They are quantitatively different, however. Comparing the scatterplots of latent heat flux versus SST, the ratio of the slope in the aerosol case to that in the greenhouse gas case is similar in the tropics and globally, on the order of a factor of 2 in both cases, but both slopes are substantially larger—again by factors between 2 and 3—in the tropical case versus the global mean. Examination of the radiative fluxes (cf. Figs. 6e–h and Figs. 8c,d) indicates this to be largely a consequence of much larger

changes in the tropics than globally, both in the longwave and shortwave. In the case of the shortwave, the differences in the aerosol and greenhouse gas cases between the tropics and globally are not individually as large as are the changes in the longwave, but the difference between the aerosol and greenhouse gas changes is again larger by about a factor of 2 in the tropics than globally.

Finally, in the interest of understanding the similarities and differences between the global and tropical responses to different radiative forcing agents further, Fig. 11 shows changes in the TOA radiative fluxes, in the same format as Figs. 6 and 9, both for the tropics and globally. As above, our sign convention is that all fluxes are positive down.

Figure 11e shows that in the aerosol experiments, TOA longwave flux decreases with SST in the global mean, consistent with dominance of the Planck and
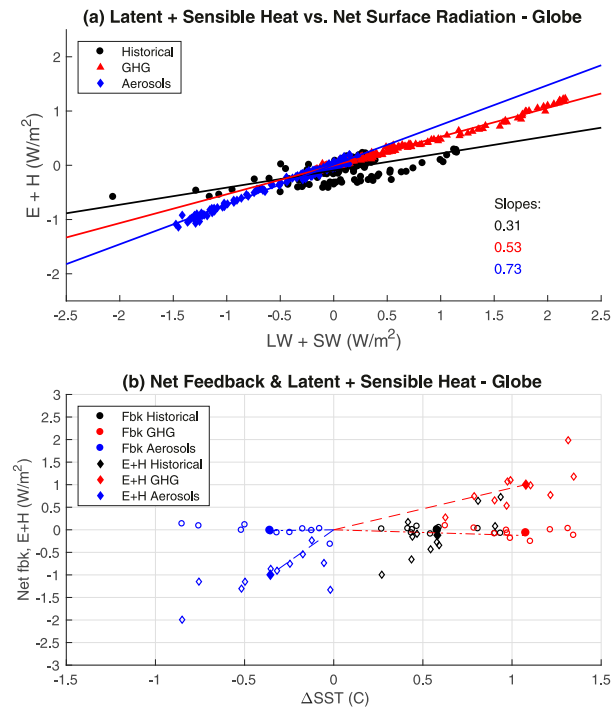
FIG. 10. (a) Global mean net surface radiative flux (shortwave plus longwave; horizontal axis) vs the sum of global mean latent and sensible heat fluxes (vertical axis); that is, as in Fig. 4, but for the globe. (b) As in Fig. 8, but for the global and annual mean.

lapse rate feedbacks over the increasing greenhouse effect associated with increasing water vapor. Net TOA radiation increases slightly with SST, consistent with the SST changes being radiatively forced, since the positive changes in shortwave TOA flux slightly exceed the negative changes in longwave. This is true as well, though with quantitatively smaller slopes for both longwave and shortwave, in the greenhouse gas experiments (Figs. 11e,f): longwave flux decreases with SST while shortwave increases slightly more. That the net TOA longwave change is negative even in these experiments, where increases in greenhouse gas concentrations are unquestionably the ultimate cause of the warming, may seem counterintuitive, but has been explained previously (Trenberth and Fasullo 2009; Donohoe et al. 2014).

Comparing Figs. 11a and 11c with Fig. 11e, in the aerosol case we see much greater scatter in the tropics than globally, and in the Northern Hemisphere, a much smaller slope, suggesting that the water vapor feedback is more competitive with the Planck and lapse rate feedbacks in that case. In the greenhouse gas experiments, the slopes become clearly positive in the tropics; the water vapor feedback combined with the direct radiative forcing from increasing greenhouse gases dominates. In the shortwave, tropical and global results

(Figs. 11b and 11d compared with Fig. 11f) show less distinct differences apart from greater scatter in the tropics.

4. Comment on temperature dependence

The CMIP5 results here and in Sobel et al. (2016) appear at first glance consistent with those of Emanuel and Sobel (2013) in that shortwave forcing has a greater influence than longwave forcing on PI per degree SST change. However, close inspection of Fig. 2 in Emanuel and Sobel (2013) shows that, in their radiative-convective equilibrium calculations, the difference emerges only when SST exceeds around 29°C, higher than the mean values over the regions of interest here. We expect the difference between shortwave and longwave forcings to become greater at sufficiently high SST, since at sufficiently high SST the net surface longwave flux will approach zero as the atmospheric boundary layer becomes very opaque in the longwave while the SST and near-surface atmospheric temperatures are nearly equal. Then further increases in greenhouse gases will have no effect at the surface, and all temperature-dependent longwave feedbacks will approximately vanish there for any forced climate change, while changes in shortwave will still have a substantial temperature-independent effect (though muted somewhat by absorption in the troposphere). This is seen in simulations of precipitation changes in response to changes in tropospheric longwave opacity (representing concentrations of all greenhouse gases including water vapor) over a wide range of climates in an idealized general circulation model (O'Gorman and Schneider 2008; O'Gorman et al. 2012), where precipitation increases with global mean surface temperature saturate at high temperatures.

We interpret the greater sensitivity to aerosols than greenhouse gases in the CMIP5 simulations shown above as being due to qualitatively the same physics as occurs in the higher-temperature regime in Emanuel and Sobel (2013) and (with the caveat again that ours are tropical rather than global results, making quantitative comparison more difficult) O'Gorman and Schneider (2008). Although the difference is manifest at lower SST here than in Emanuel and Sobel (2013), the precise SST at which it should emerge is expected to depend on the details of radiative transfer in both the longwave and shortwave (the latter since shortwave absorption is not negligible) and how both scale with surface temperature. These may differ in different models and experimental designs, all of which are substantially different between the studies described in this section. More detailed study of the surface energy budget's different
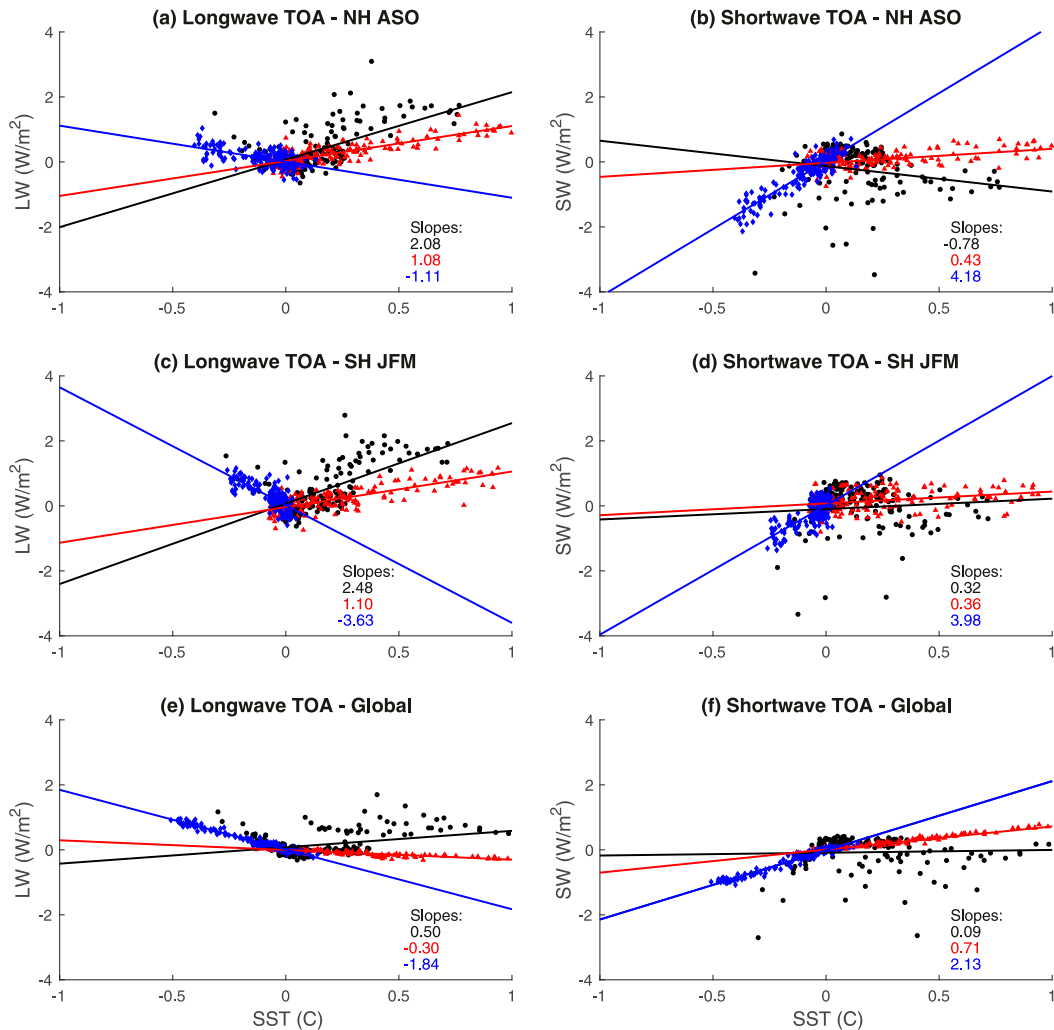
FIG. 11. Scatterplots of top-of-the-atmosphere radiative fluxes vs SST for the (a),(b) NH and (c),(d) SH tropics and (e),(f) the global and annual mean. (left) Longwave fluxes and (right) shortwave fluxes.

responses to warming as they depend on these details would be valuable.

5. Conclusions

We have analyzed single-forcing and historical CMIP5 experiments in order to understand the greater influence of aerosols compared to greenhouse gases on the potential intensity (PI) of tropical cyclones (TCs). We analyzed sea surface temperature (SST), PI, and terms in the surface energy budget over the tropical ocean regions and seasons most conducive to TCs. Our primary conclusions are as follows:

1) Using PI theory, we can decompose the PI variations into components due to thermodynamic efficiency, surface turbulent (latent plus sensible) heat fluxes,

and surface wind speed. Surface turbulent fluxes explain about half the signal in PI, while thermodynamic efficiency explains a small fraction. Surface wind speed, computed from monthly mean winds available from a subset of the models, does not explain the remainder. Further investigation of the role of surface wind speed requires high-frequency wind data and consideration of each model's parameterization of surface fluxes, and is deferred here. The rest of our interpretation focuses on the heat flux component, which is interpreted in terms of the surface energy budget, assuming that perturbations in turbulent and radiative fluxes balance.

2) Aerosols have a stronger influence than greenhouse gases on surface fluxes, and thus the component of PI that is explained by surface fluxes, because they act primarily in the shortwave part of the

electromagnetic spectrum while greenhouse gases act in the longwave.

3) Calculations with offline radiative kernels indicate that the temperature-dependent feedbacks resulting from both temperature and humidity changes are similar between aerosol-only and greenhouse gas-only experiments. This is true in both the longwave and shortwave. Thus the difference between aerosol and greenhouse gas forcings is due to the difference in the direct, temperature-independent effects of the radiative forcing agents themselves.

4) Our results concerning the surface turbulent fluxes are in most respects qualitatively similar to those from prior studies on the global hydrological cycle. Our analysis differs from those prior ones, however, in that we analyze means over the tropics of a single hemisphere in a single season, as opposed to the global and annual means used in most studies of the hydrologic cycle. Precipitation can be straightforwardly related to radiative quantities only in the global mean, whereas the relationship between latent heat flux and PI, and between latent heat flux and the other terms in the surface energy budget, is local as long as the ocean mixed layer is in an appropriately defined equilibrium on the time scales of interest. Comparison of tropical seasonal results to global annual results for the same CMIP5 experiments, at both the surface and top of atmosphere, shows a number of quantitative differences and even some qualitative ones. As an example, while the net top of atmosphere longwave radiation decreases with SST globally in the GHG experiments [so that the warming is driven by shortwave radiation changes despite the ultimate cause being greenhouse gases, as found by Trenberth and Fasullo (2009) and Donohoe et al. (2014)], it increases with SST in the tropics.

5) Results from historical simulations containing all natural and anthropogenic forcings are complex, with greater scatter in the relationships between the different quantities analyzed here. In general they resemble the greenhouse gas-only experiments more than the aerosol-only experiments, as perhaps might be expected since the greenhouse gas forcing is generally larger than the aerosol forcing over the period simulated. The latent heat flux and PI changes, however, are smaller than in the single-forcing experiments, due to the cancellation between the forcings that motivated this study. A more in-depth study of the degree to which the response to the combined forcings is or is not linear (and thus predictable from knowing the single-forcing results) would be valuable, but would be best carried out in simulations where the forcings are known.

REFERENCES

Allen, M. R., and W. J. Ingram, 2002: Constraints on future changes in climate and the hydrologic cycle. *Nature*, **419**, 224–232, https://doi.org/10.1038/nature01092.

Andrews, T., P. M. Forster, and J. M. Gregory, 2009: A surface energy perspective on climate change. *J. Climate*, **22**, 2557–2570, https://doi.org/10.1175/2008JCLI2759.1.

Bala, G., P. B. Duffy, and K. E. Taylor, 2008: Impact of geo-engineering schemes on the global hydrological cycle. *Proc. Natl. Acad. Sci. USA*, **105**, 7664–7669, https://doi.org/10.1073/pnas.0711648105.

Bister, M., and K. A. Emanuel, 1998: Dissipative heating and hurricane intensity. *Meteor. Atmos. Phys.*, **50**, 233–240, https://doi.org/10.1007/BF01030791.

——, and ——, 2002: Low frequency variability of tropical cyclone potential intensity 1. Interannual to interdecadal variability. *J. Geophys. Res.*, **107**, 4801, https://doi.org/10.1029/2001JD000776.

Booth, B. B. B., N. J. Dunstone, P. R. Halloran, T. Andrews, and N. Bellouin, 2012: Aerosols implicated as a prime driver of twentieth-century North Atlantic climate variability. *Nature*, **484**, 228–232, https://doi.org/10.1038/nature10946.

Boucher, O., and Coauthors, 2013: Clouds and aerosols. *Climate Change 2013: The Physical Science Basis*, T. F. Stocker et al., Eds., Cambridge University Press, 571–657.

Bryan, G. H., and R. Rotunno, 2009a: Evaluation of an analytical model for the maximum intensity of tropical cyclones. *J. Atmos. Sci.*, **66**, 3042–3060, https://doi.org/10.1175/2009JAS3038.1.

——, and ——, 2009b: The maximum intensity of tropical cyclones in axisymmetric numerical model simulations. *Mon. Wea. Rev.*, **137**, 1770–1789, https://doi.org/10.1175/2008MWR2709.1.

Donohoe, A., K. C. Armour, A. G. Pendergrass, and D. S. Battisti, 2014: Radiative feedbacks on global precipitation. *Proc. Natl. Acad. Sci. USA*, **111**, 16 700–16 705, https://doi.org/10.1073/pnas.1412190111.

Dunstone, N. J., D. M. Smith, B. B. B. Booth, L. Hermanson, and R. Eade, 2013: Anthropogenic aerosol forcing of Atlantic tropical storms. *Nat. Geosci.*, **6**, 534–539, https://doi.org/10.1038/ngeo1854.

Emanuel, K. A., 1986: An air-sea interaction theory for tropical cyclones. Part I: Steady-state maintenance. *J. Atmos. Sci.*, **43**, 585–605, https://doi.org/10.1175/1520-0469(1986)043<0585:AASITF>2.0.CO;2.

——, 1995: The behavior of a simple hurricane model using a convective scheme based on subcloud-layer entropy equilibrium. *J. Atmos. Sci.*, **52**, 3960–3968, https://doi.org/10.1175/1520-0469(1995)052<3960:TBOASH>2.0.CO;2.

——, 2000: A statistical analysis of tropical cyclone intensity. *Mon. Wea. Rev.*, **128**, 1139–1152, https://doi.org/10.1175/1520-0493(2000)128<1139:ASAOTC>2.0.CO;2.

——, 2007: Environmental factors affecting tropical cyclone power dissipation. *J. Climate*, **20**, 5497–5509, https://doi.org/10.1175/2007JCLI1571.1.

——, and R. Rotunno, 2011: Self-stratification of tropical cyclone outflow. Part I: Implications for storm structure. *J. Atmos. Sci.*, **68**, 2236–2249, https://doi.org/10.1175/JAS-D-10-05024.1.

——, and A. H. Sobel, 2013: Response of tropical sea surface temperature, precipitation, and tropical cyclone-related variables to changes in global and local forcing. *J. Adv. Model. Earth Syst.*, **5**, 447–458, https://doi.org/10.1002/jame.20032.

Feichter, J., and E. Roeckner, 2004: Nonlinear aspects of the climate response to greenhouse gas and aerosol forcing. *J. Climate*, **17**, 2384–2398, https://doi.org/10.1175/1520-0442(2004)017<2384:NAOTCR>2.0.CO;2.

Gregory, J. M., and P. M. Forster, 2008: Transient climate response estimated from radiative forcing and observed temperature change. *J. Geophys. Res.*, **113**, D23105, https://doi.org/10.1029/2008JD010405.

——, and Coauthors, 2004: A new method for diagnosing radiative forcing and climate sensitivity. *Geophys. Res. Lett.*, **31**, L03205, https://doi.org/10.1029/2003GL018747.

Hausman, S. A., K. V. Ooyama, and W. H. Schubert, 2006: Potential vorticity structure of simulated hurricanes. *J. Atmos. Sci.*, **63**, 87–108, https://doi.org/10.1175/JAS3601.1.

Held, I. M., M. Winton, K. Takahashi, T. Delworth, F. Zeng, and G. K. Vallis, 2010: Probing the fast and slow components of global warming by returning abruptly to preindustrial forcing. *J. Climate*, **23**, 2418–2427, https://doi.org/10.1175/2009JCLI3466.1.

Hung, M.-P., J.-L. Lin, W. Wang, D. Kim, T. Shinoda, and S. J. Weaver, 2013: MJO and convectively coupled equatorial waves simulated by CMIP5 climate models. *J. Climate*, **26**, 6185–6214, https://doi.org/10.1175/JCLI-D-12-00541.1.

Liepert, B. G., and M. Previdi, 2009: Do models and observations disagree on the rainfall response to global warming? *J. Climate*, **22**, 3156–3166, https://doi.org/10.1175/2008JCLI2472.1.

Mann, M. E., and K. A. Emanuel, 2006: Atlantic hurricane trends linked to climate change. *Eos, Trans. Amer. Geophys. Union*, **87**, 233–241, https://doi.org/10.1029/2006EO240001.

Marvel, K., G. A. Schmidt, D. Shindell, C. Bonfils, A. N. LeGrande, L. Nazarenko, and K. Tsigaridis, 2015: Do responses to different anthropogenic forcings add linearly in climate models? *Environ. Res. Lett.*, **10**, 104010, https://doi.org/10.1088/1748-9326/10/10/104010.

O'Gorman, P., and T. Schneider, 2008: The hydrological cycle over a wide range of climates simulated with an idealized GCM. *J. Climate*, **21**, 524–535, https://doi.org/10.1175/2007JCLI2065.1.

——, R. P. Allan, M. P. Byrne, and M. Previdi, 2012: Energetic constraints on precipitation under climate change. *Surv. Geophys.*, **33**, 585–608, https://doi.org/10.1007/s10712-011-9159-6.

Persing, J., and M. T. Montgomery, 2003: Hurricane superintensity. *J. Atmos. Sci.*, **60**, 2349–2371, https://doi.org/10.1175/1520-0469(2003)060<2349:HS>2.0.CO;2.

Previdi, M., 2010: Radiative feedbacks on global precipitation. *Environ. Res. Lett.*, **5**, 025211, https://doi.org/10.1088/1748-9326/5/2/025211.

——, and B. G. Liepert, 2012: The vertical distribution of climate forcings and feedbacks from the surface to top of atmosphere. *Climate Dyn.*, **39**, 941–951, https://doi.org/10.1007/s00382-011-1233-8.

Reichler, T., M. Dameris, and R. Sausen, 2003: Determining the tropopause height from gridded data. *Geophys. Res. Lett.*, **30**, 2042, https://doi.org/10.1029/2003GL018240.

Roeckner, E., and Coauthors, 2003: The atmospheric general circulation model ECHAM5—Part I: Model description. Tech. Rep. 349, Max-Planck-Institut für Meteorologie, Hamburg, Germany, 127 pp.

Samset, B. H., and Coauthors, 2016: Fast and slow precipitation responses to individual climate forcers: A PDRMIP multi-model study. *Geophys. Res. Lett.*, **43**, 2782–2791, https://doi.org/10.1002/2016GL068064.

Shindell, D. T., and Coauthors, 2013: Radiative forcing in the ACCMIP historical and future climate simulations. *Atmos. Chem. Phys.*, **13**, 2939–2974, https://doi.org/10.5194/acp-13-2939-2013.

Sobel, A. H., S. J. Camargo, T. M. Hall, C.-Y. Lee, M. K. Tippett, and A. A. Wing, 2016: Human influence on tropical cyclone intensity. *Science*, **353**, 242–246, https://doi.org/10.1126/science.aaf6574.

Soden, B. J., I. M. Held, R. Colman, K. M. Shell, J. T. Kiehl, and C. A. Shields, 2008: Quantifying climate feedbacks using radiative kernels. *J. Climate*, **21**, 3504–3520, https://doi.org/10.1175/2007JCLI2110.1.

Taylor, K. E., R. J. Stouffer, and G. A. Meehl, 2012: An overview of CMIP5 and the experiment design. *Bull. Amer. Meteor. Soc.*, **93**, 485–498, https://doi.org/10.1175/BAMS-D-11-00094.1.

Ting, M., S. J. Camargo, C. Li, and Y. Kushnir, 2015: Natural and forced North Atlantic hurricane potential intensity change in CMIP5 models. *J. Climate*, **28**, 3926–2942, https://doi.org/10.1175/JCLI-D-14-00520.1.

Trenberth, K. E., and J. T. Fasullo, 2009: Global warming due to increasing absorbed solar radiation. *Geophys. Res. Lett.*, **36**, L07706, https://doi.org/10.1029/2009GL037527.

Wang, S., S. J. Camargo, A. H. Sobel, and L. M. Polvani, 2014: Impact of the tropopause temperature on the intensity of tropical cyclones: An idealized study using a mesoscale model. *J. Atmos. Sci.*, **71**, 4333–4348, https://doi.org/10.1175/JAS-D-14-0029.1.

Wing, A. A., A. H. Sobel, and S. J. Camargo, 2007: Relationship between the potential and actual intensities of tropical cyclones on interannual time scales. *Geophys. Res. Lett.*, **34**, L08810, https://doi.org/10.1029/2006GL028581.